Supporting Information

Halogenated Carborane Molecular Ferroelectric Crystals with High-Temperature Phase Transition

Wenjing Guo, Wenkang Cheng, Yuting Li, Zhenhong Wei*, Hu Cai*

School of Chemistry and Chemical Engineering, Nanchang University, Nanchang City, 330031, P.R. China.

*Corresponding emails: weizh@ncu.edu.cn, caihu@ncu.edu.cn

Experimental Section

Materials. Trifluoromethanesulfonic acid (219 μL, 2.5 mmol) was introduced into the reaction mixture comprising *o*-carborane (720 mg, 5 mmol) and *N*-bromosuccinimide (978 mg, 5.5 mmol) in 50 mL of hexafluoroisopropanol (HFIP). Subsequently, the reaction mixture was stirred at room temperature for 40 minutes. Upon completion of the reaction, HFIP was recovered by distillation, followed by extraction with ethyl acetate (50 mL × 3). The combined organic phase was dried over anhydrous Na_2SO_4, and concentrated under vacuum. The crude mixture was subjected to chromatographic purification, resulting in the isolation of **1** (eluent: pentane/ethyl acetate = 8/1, R_f = 0.2). Yield: 1.04 g, 94%. The synthesis process of **2** closely parallels, with the exception that trichloroisocyanuric acid (TCCA) was employed as the chlorinating reagent.

Trifluoromethanesulfonic acid (878 μL, 10 mmol) was introduced into the reaction system containing o-carborane (720 mg, 5 mmol) and NBS (1868 mg, 10.5 mmol) in HFIP (50 mL). The reaction mixture was then stirred at room temperature for 1 hour. Upon completion of the reaction, HFIP was recovered via distillation, and the residue was extracted with ethyl acetate (50 mL × 3). The combined organic layers were dried over anhydrous Na_2SO_4 and concentrated under reduced pressure. The crude product was purified by chromatography, yielding compound **4** (eluent: pentane/ethyl acetate = 8/1, R_f = 0.2) with a 90% yield. The chlorination reagent used was TCCA, and the synthesis of compounds **3** and **5** was performed using similar methods, with compounds **2** and *o*-carborane as the respective substrates.

Thin-Film Preparation. Prior to use, indium tin oxide (ITO) glass was preliminarily cleaned with water, ethanol, and acetone. Crystalline samples **1–5** (each 10 mg) were dissolved in 200 μL of ethyl acetate or dichloromethane. 20 μL of the solution was spin-coated onto the cleaned ITO glass substrates. The solvent was allowed to gradually evaporate at room temperature, resulting in the formation of polycrystalline thin films.

Measurement Methods

Single-crystal and powder X-ray crystallography.

X-ray single-crystal diffraction experiments were performed utilizing a Rigaku Saturn 924 diffractometer, outfitted with Mo-Kα radiation (λ = 0.71073 Å). X-ray diffraction (XRD) analyses were executed employing a PANalytical X'Pert3 diffractometer, equipped with a Cu Kα X-ray source (λ = 1.5418 Å, 40 kV, 150 mA), with a scan rate set at 10° min^{-1} for the measurements.

Thermal analyses.

Differential scanning calorimetry (DSC) measurements were performed with a NETZSCH DSC 200F3 instrument. Crystalline samples underwent both heating and cooling processes at a consistent rate of 20 K min^{-1} under aluminum crucibles and nitrogen atmosphere.

SHG and dielectric measurements.

The second harmonic generation (SHG) was examined using INSTEC instruments. Complex dielectric permittivities were assessed utilizing the DMS-1000 dielectric temperature spectrum measuring system. Silver conductive paste was utilized to coat the surfaces of the samples, serving dual roles as the top and bottom electrodes.

PFM characterization.

The PFM measurements were performed utilizing a piezoresponse force microscopy (PFM) system, specifically the Oxford instrument Cypher ES, equipped with a high-voltage package. PFM is a technique derived from atomic force microscopy (AFM), which involves the application of an AC drive voltage to the conductive tip. In our study, we employed conductive Pt/Ir-coated silicon probes (EFM, Nanoworld) with a nominal spring constant of approximately 2.8 nN/nm and a free-air resonance frequency of approximately 75 kHz. The PFM experiments were conducted in Dual Frequency Tracking mode, enabling domain imaging and investigation of polarization switching behaviors.

IR measurements.

The Fourier transform infrared (FTIR) spectra were acquired employing the Bruker Alpha II instrument.

Computing methods.

The calculation of dipole moments was conducted using density functional theory (DFT). DFT computations were carried out employing the Gaussian 09 suite of programs (Wallingford, CT, 2013), utilizing the B3LYP functional in conjunction with the 6-311G** basis set.

NMR measurements.

The ^{1}H and ^{13}C nuclear magnetic resonance (NMR) spectra were obtained using a Bruker Advance III 400 spectrometer (400 MHz for ^{1}H, 100 MHz for ^{13}C, and 128 MHz for ^{11}B NMR). The samples were dissolved either in $CDCl_3$ or CD_3CN, with tetramethylsilane (TMS) serving as the internal reference standard. Chemical shifts (δ) were recorded in parts per million (ppm) and referenced to TMS (δ = 0) for ^{1}H, chloroform (δ = 77.0) for ^{13}C, and acetonitrile (δ = 118.26) for ^{13}C as internal standards. For ^{11}B and $^{11}B\{^{1}H\}$ NMR spectra, data were calibrated using external boron trifluoride diethyl ether ($BF_3{\cdot}Et_2O$) as the reference compound.

Characterization data.

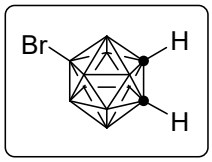

1: White solid, 94%; **^{1}H NMR (400 MHz, CD_3CN)**: δ 3.60 (s, 2H); **^{1}H{^{11}B} NMR (400 MHz, $CDCl_3$)**: δ 3.59 (s, 2H), 2.68 (s, 1H), 2.55 (s, 2H), 2.49 (s, 2H), 2.34 (s, 2H), 2.16 (s, 2H). **^{13}C{^{1}H} NMR (100 MHz, CD_3CN)**: δ 53.26, 46.77; **^{11}B NMR (128 MHz, CD_3CN)**: δ 0.16 (s, 1B), -1.58 (d, *J* = 152.3 Hz, 1B), -8.27 (d, *J* = 154.9 Hz, 2B), -12.86 – -16.41 (m, 6B); **^{11}B{^{1}H} NMR (128 MHz, CD_3CN)**: δ 0.21 (1B), -1.51 (1B), -8.25 (2B), -13.49 (2B), -14.47 (2B), -15.70 (2B).

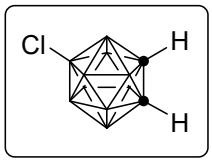

2: White solid, 72%; **^{1}H NMR (400 MHz, $CDCl_3$)**: δ 3.55 (s, 1H), 3.43 (s, 1H); **^{1}H{^{11}B} NMR (400 MHz, $CDCl_3$)**: δ 3.55 (s, 1H), 3.43 (s, 1H), 2.60 (s, 1H), 2.47 (s, 2H), 2.41 (s, 2H), 2.29 (s, 2H), 2.11 (s, 2H); **^{13}C{^{1}H} NMR (100 MHz, $CDCl_3$)**: δ 52.03, 44.31; **^{11}B NMR (128 MHz, $CDCl_3$)**: δ 7.59 (s, 1B), -1.96 (d, *J* = 153.6 Hz, 1B), -8.73 (d, *J* = 156.1 Hz, 2B), -13.21 – -17.07 (m, 6B); **^{11}B{^{1}H} NMR (128 MHz, $CDCl_3$)**: δ 7.70 (1B), -1.89 (1B), -8.67 (2B), -13.83 (2B), -15.15 (2B), -16.35 (2B).

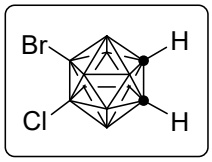

3: White solid, 92%; **^{1}H NMR (400 MHz, $CDCl_3$)**: δ 3.63 (s, 1H), 3.52 (s, 1H); **^{1}H{^{11}B} NMR (400 MHz, $CDCl_3$)**: δ 3.62 (s, 1H), 3.51 (s, 1H), 2.64 (s, 2H), 2.47 (s, 4H), 2.31 (s, 2H); **^{13}C{^{1}H} NMR (100 MHz, $CDCl_3$)**: δ 45.46, 44.22; **^{11}B NMR (128 MHz, $CDCl_3$)**: δ 7.04 (s, 1B), 0.09 (s, 1B), -7.78 (d, *J* = 154.9 Hz, 2B), -14.81 (d, *J* = 168.9 Hz, 4B), -17.60 (d, *J* = 180.5 Hz, 2B); **^{11}B{^{1}H} NMR (128 MHz, $CDCl_3$)**: δ 7.04 (1B), 0.10 (1B), -7.76 (2B), -14.79 (4B), -17.63 (2B).

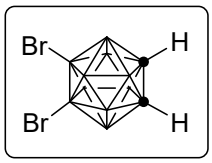

4: White solid, 80%; **^{1}H NMR (400 MHz, $CDCl_3$)**: δ 3.70 (s, 2H); **^{1}H{^{11}B} NMR (400 MHz, $CDCl_3$)**: δ 3.70 (s, 2H), 2.69 (s, 2H), 2.54 (s, 4H), 2.37 (s, 2H); **^{13}C7{^{1}H} NMR (100 MHz, $CDCl_3$)**: δ 46.49; **^{11}B NMR (128 MHz, $CDCl_3$)**: δ 0.19 (s, 2B), -7.42 (d, *J* = 152.3 Hz, 2B), -14.46 (d, *J* = 166.4 Hz, 4B), -16.99 (d, *J* = 189.4 Hz, 2B); **^{11}B{^{1}H} NMR (128 MHz, $CDCl_3$)**: δ 0.27 (2B), -7.40 (2B), -14.49 (4B), -17.03 (2B).

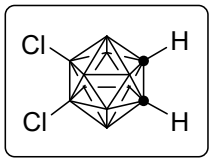

5: White solid, 77%; **^{1}H NMR (400 MHz, $CDCl_3$)**: δ 3.48 (s, 2H); **^{1}H{^{11}B} NMR (400 MHz, $CDCl_3$)**: δ 3.47 (s, 2H), 2.57 (s, 2H), 2.41 (s, 4H), 2.26 (s, 2H); **^{13}C{^{1}H} NMR (100 MHz, $CDCl_3$)**: δ 43.32; **^{11}B NMR (128 MHz, $CDCl_3$)**: δ 6.86 (s, 2B), -8.29 (d, *J* = 156.2 Hz, 2B), -15.28 (d, *J* = 168.9 Hz, 4B), -18.41 (d, *J* = 185.6 Hz, 2B); **^{11}B{^{1}H} NMR (128 MHz, $CDCl_3$)**: δ 6.96 (2B), -8.26 (2B), -15.28 (4B), -18.42 (2B).

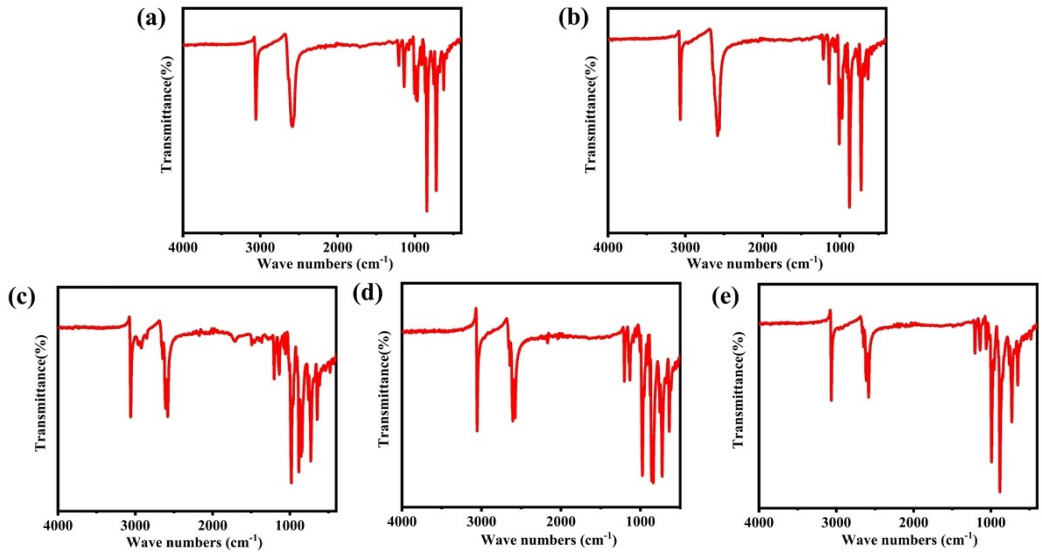

Figure S1. Experimental IR absorption spectra of **1–5** (a-e) under ambient condition.

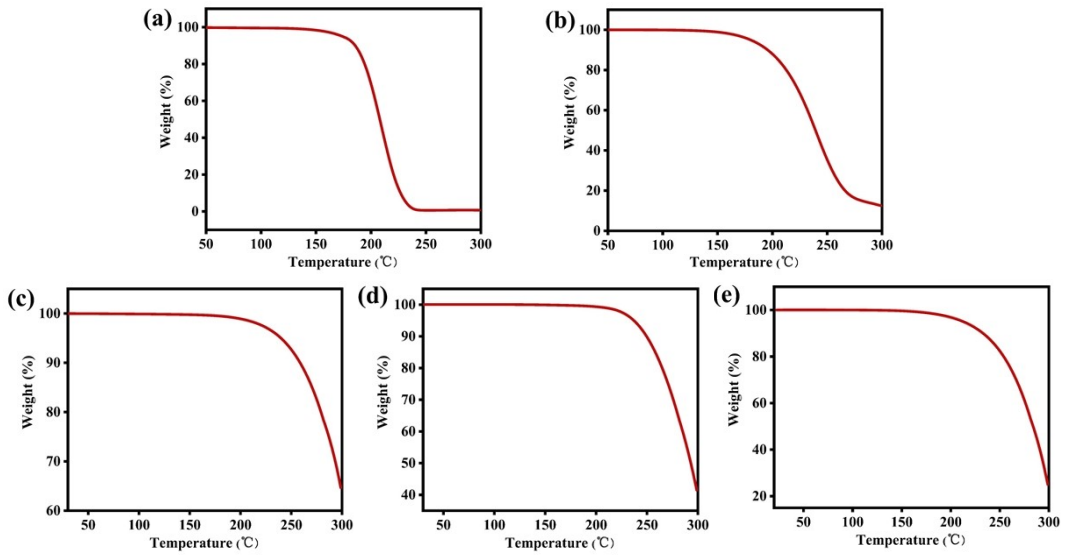

Figure S2. TGA of **1–5** (a-e)**.**

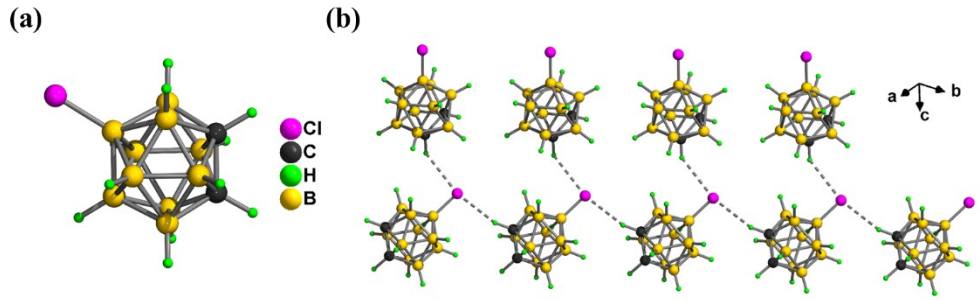

Figure S3. The crystal structures of **2**.

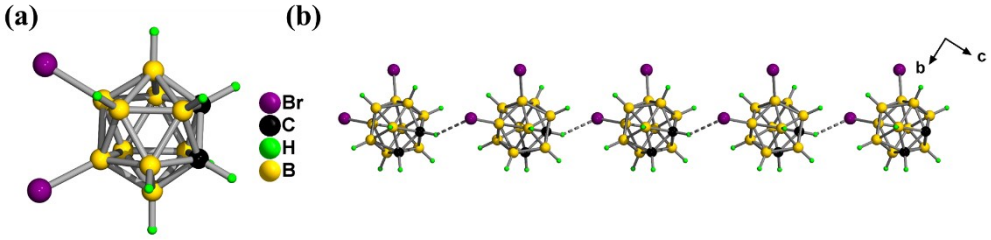

Figure S4. The crystal structures of **4**.

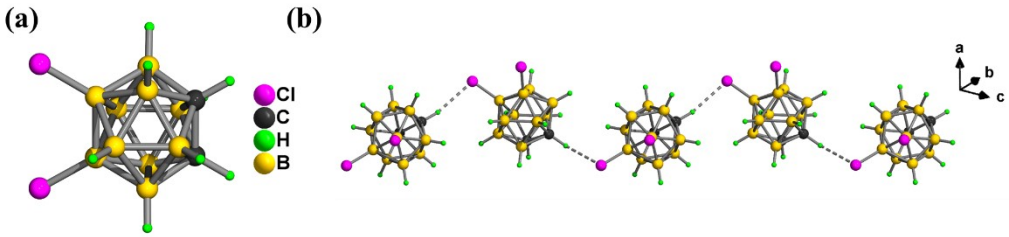

Figure S5. The crystal structures of **5**.

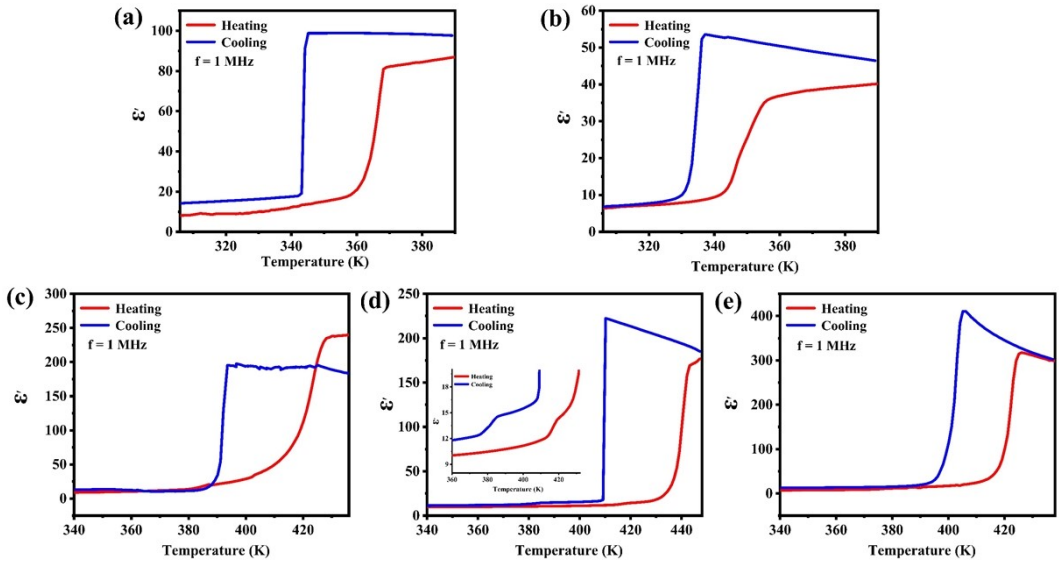

Figure S6. Temperature-dependent ε' of **1–5** (a-e) at 1 MHz.

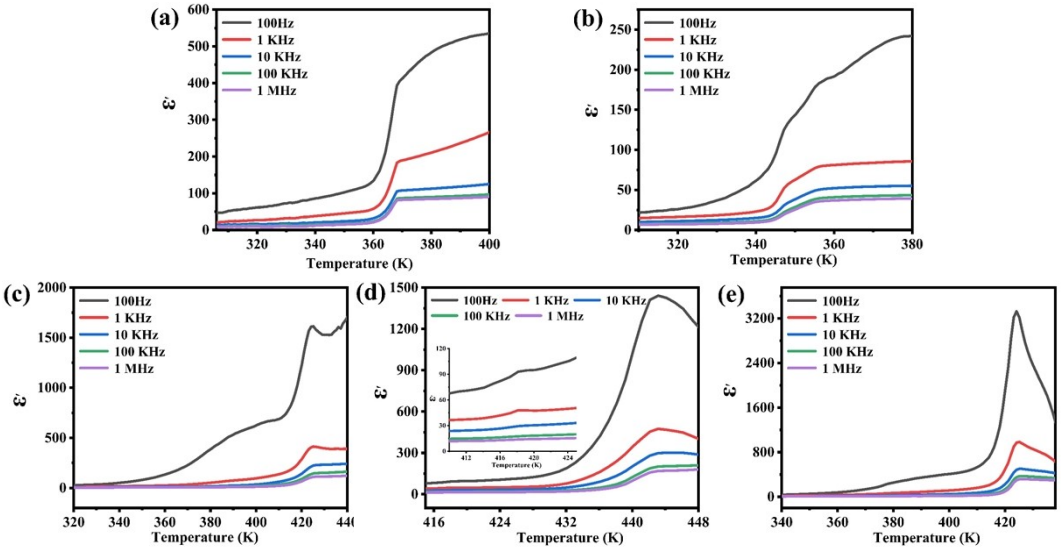

Figure S7. The real part ε' at different frequencies of **1–5** (a-e).

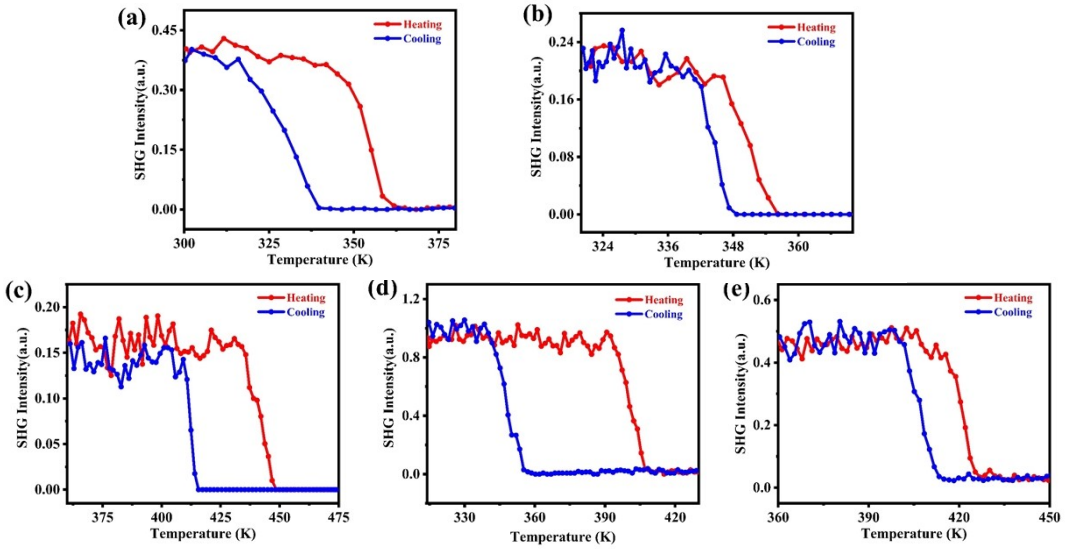

Figure S8. Temperature-dependent SHG intensity of **1**–**5** (a-e).

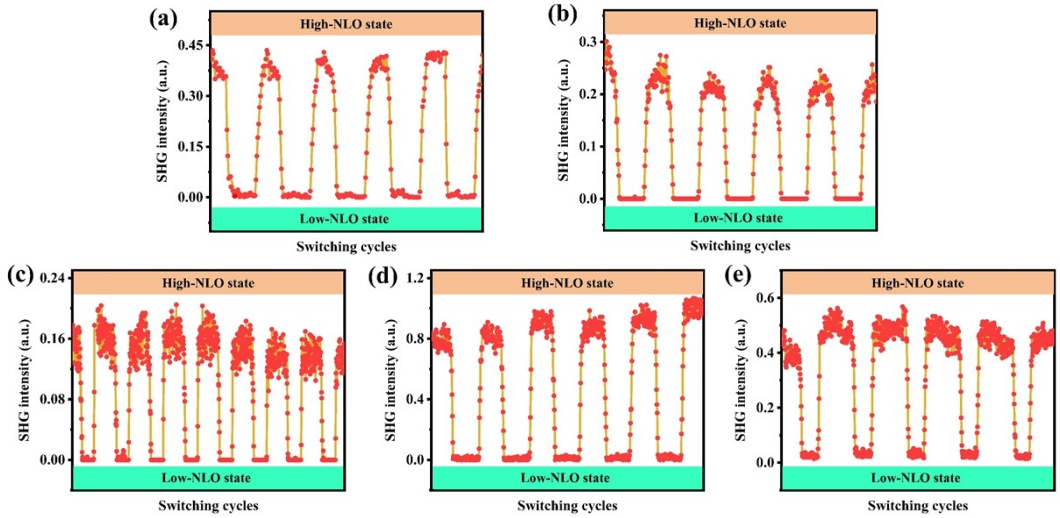

Figure S9. Switching SHG cycles of **1**–**5** (a-e).

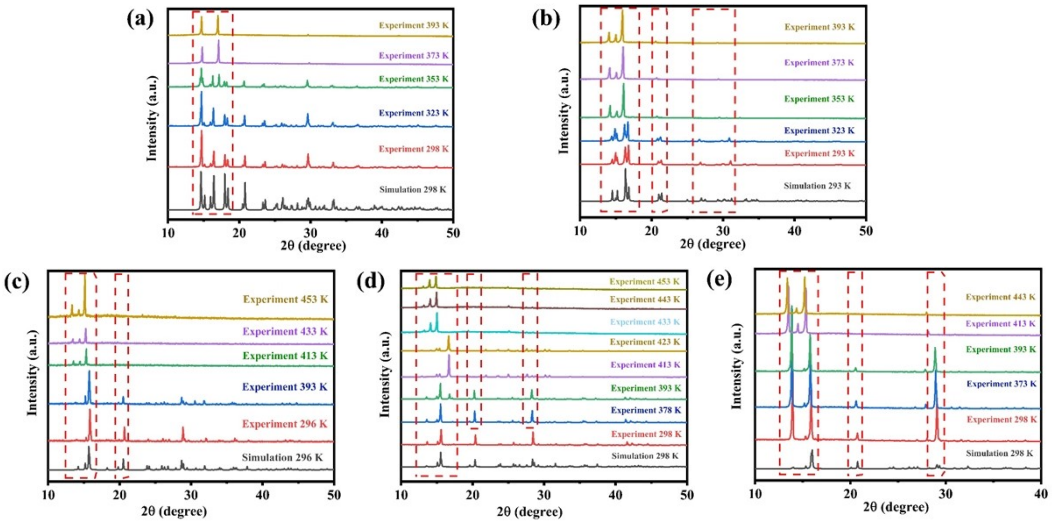

Figure S10. Variable-temperature PXRD patterns of **1**–**5** (a-e).

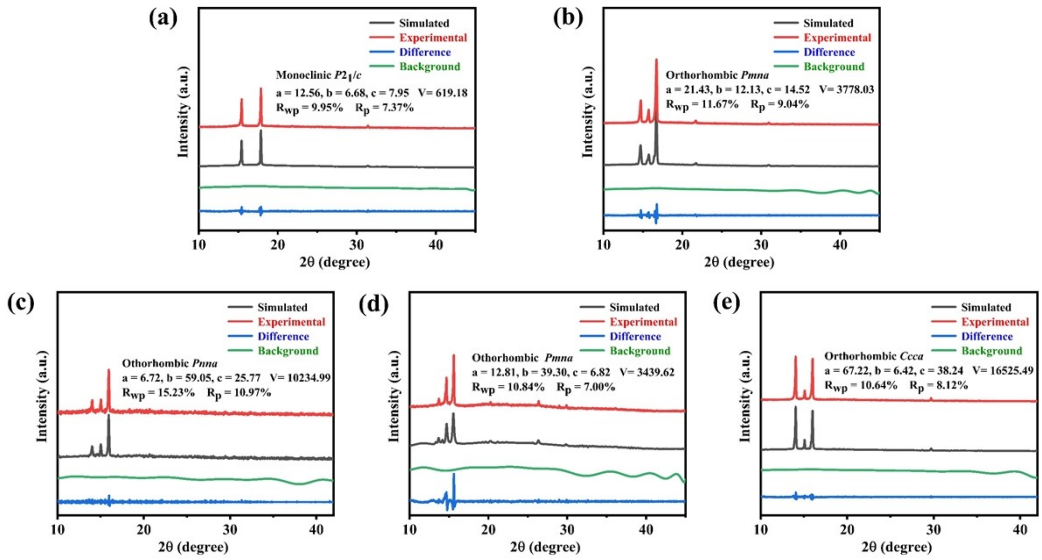

Figure S11. Pawley refinement of PXRD data of **1–5** (a–e) collected at high temperature.

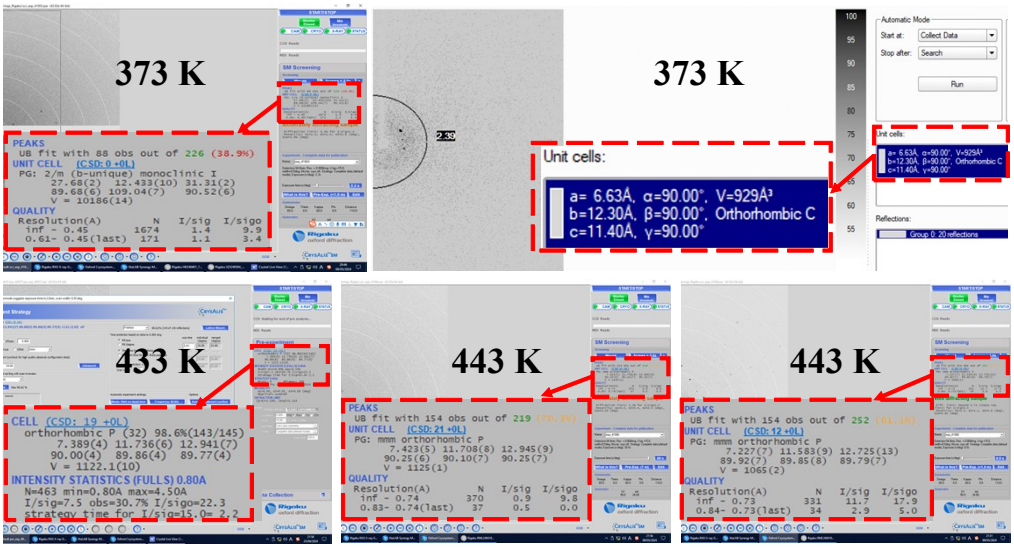

Figure S12. Single crystal X-ray diffraction pattern of **1–5** at 373 K, 373 K, and 433 K, 443 K and 443 K, respectively.

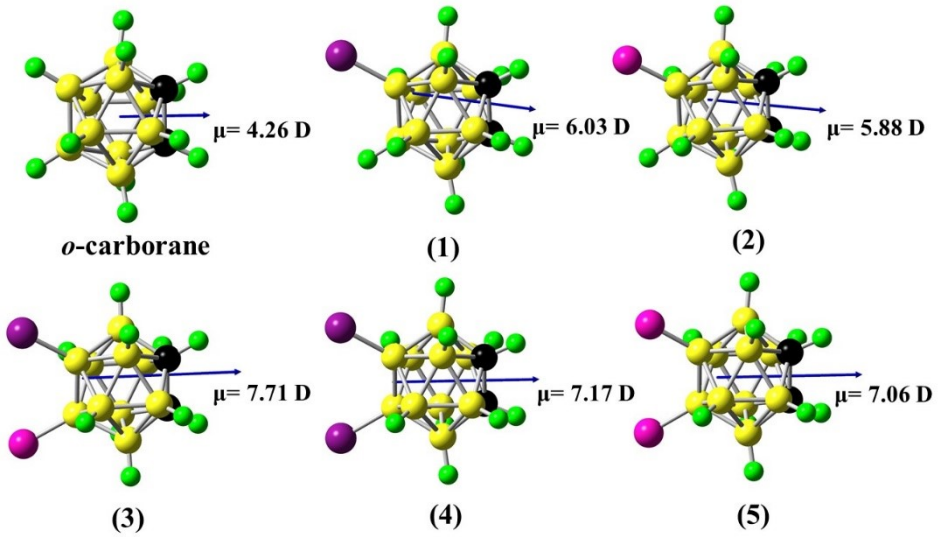

Figure S13. The dipole moments calculated for *o*-carborane and compounds **1–5**.

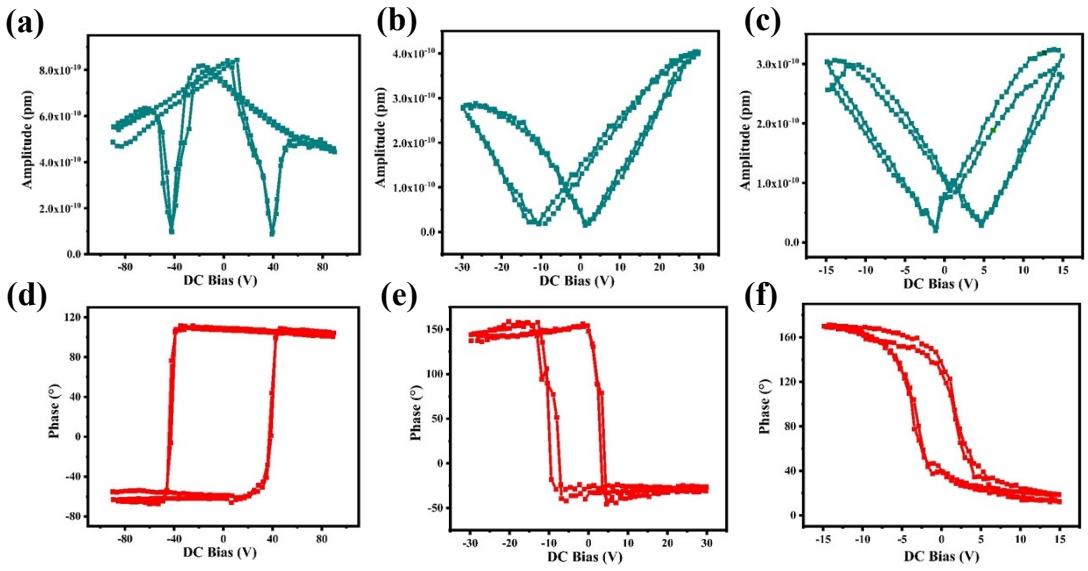

Figure S14. PFM amplitude (a, b, c) and phase hysteresis loops (d, e, f) of **2**, **4** and **5** thin films.

Table S1. Crystal data and structure refinement for 1-2.

Formula	$C_2H_{12}B_{10}Br$	$C_2H_{12}B_{10}Cl$
Temperature	296 K	296 K
Formula weight	223.11	178.66
Crystal system	monoclinic	monoclinic
Space group	$P2_1$	*Cc*
a (Å)	6.8936(14)	7.119(6)
b (Å)	24.047(5)	11.824(6)
c (Å)	7.1162(15)	11.636(8)
V(Å)^3	1035.6(4)	979.4(12)
Z	4	4
D_{calc} (g.cm^{-3})	1.431	1.212
F(000)	432.0	360.0
ϑ_{max}	27.530	27.882
μ(Mo Ka,mm^{-1})	3.900	0.316
Reflections collected	6221	2725
Unique reflections	4764 [$R_{(int)}$ = 0.0368]	2327 [$R_{(int)}$ = 0.0335]
No. of variables	236	119
Final *R* indices ($I \geq 2\sigma$)	R_1 = 0.0633, wR_2 = 0.1492	R_1 = 0.0603, wR_2 = 0.1298
R indices (all data)	R_1 = 0.0957, wR_2 = 0.1631	R_1 = 0.0775, wR_2 = 0.1427
Goodness-of-fit	1.058	1.113

Table S2. Crystal data and structure refinement for 3-5.

Formula	$C_2H_{10}B_{10}BrCl$	$C_2H_{10}B_{10}Br_2$	$C_2H_{10}B_{10}Cl_2$
Temperature	296 K	293 K	296 K
Formula weight	257.55	302.02	213.10
Crystal system	orthorhombic	orthorhombic	orthorhombic
Space group	$Pna2_1$	$Pna2_1$	$Pna2_1$
a (Å)	12.9028(15)	13.0415(7)	12.7212(14)
b (Å)	7.3660(8)	7.4431(4)	7.2601(8)
c (Å)	11.6524(13)	11.7318(6)	11.5565(14)
V(Å)^3	1107.5(2)	1138.80(10)	1067.3(2)
Z	4	4	4
D_{calc} (g.cm^{-3})	1.545	1.762	1.326
F(000)	496.0	568.0	424.0
ϑ_{max}	24.998	30.771	27.640
μ(Mo Ka,mm^{-1})	3.891	7.058	0.544
Reflections collected	5262	5594	6096
Unique reflections	1953 [$R_{(int)}$ = 0.0244]	3552 [$R_{(int)}$ = 0.0333]	2496 [$R_{(int)}$ = 0.0219]
No. of variables	128	127	127
Final R indices ($I \geq 2\sigma$)	R_1 = 0.0638, wR_2 = 0.1984	R_1 = 0.0362, wR_2 = 0.1006	R_1 = 0.0357, wR_2 = 0.0901
R indices (all data)	R_1 = 0.0682, wR_2 = 0.2054	R_1 = 0.0475, wR_2 = 0.1081	R_1 = 0.0412, wR_2 = 0.0936
Goodness-of-fit	1.085	0.797	1.057

Table S3. Hydrogen bond lengths [Å] and bond angles [°] of 1 at LTP.

D-H···A	D-H [Å]	H···A[Å]	D···A[Å]	D-H···A[°]
B(9)-H(9)···Br(1)[1]	1.10	2.70	3.651(18)	145
B(13)-H(13)···Br(2)[2]	1.10	2.86	3.763(15)	139
C(2)-H(2)···Br(2)[3]	1.10	2.81	3.794(9)	149
C(3)-H(3)···Br(1)	1.10	2.79	3.680(9)	137

Symmetry codes: [1] -1+*x*, *y*, *z*; [2] *x*, *y*, -1+*z*; [3] 1-*x*, 1/2+*y*, 1-*z*

Table S4. Hydrogen bond lengths [Å] and bond angles [°] of 2 at LTP.

D-H···A	D-H [Å]	H···A[Å]	D···A[Å]	D-H···A[°]
C(1)-H(1)···Cl(1)[1]	1.10	2.64	3.579(7)	143
C(2)-H(2)···Cl(1)[2]	1.10	2.77	3.619(7)	134

Symmetry codes: [1] 1/2+*x*, 1/2+*y*, *z*; [2] 1/2+*x*, 3/2-*y*, 1/2+*z*.

Table S5. Hydrogen bond lengths [Å] and bond angles [°] of 3 at LTP.

D-H···A	D-H [Å]	H···A[Å]	D···A[Å]	D-H···A[°]
C(1)-H(1)···Cl(1)[1]	1.10	2.59	3.600(11)	153

Symmetry codes: [1] 3/2-*x*, 1/2+*y*, -1/2+*z*.

Table S6. Hydrogen bond lengths [Å] and bond angles [°] of 4 at LTP.

D-H···A	D-H [Å]	H···A[Å]	D···A[Å]	D-H···A[°]
C(4)-H(4)···Br(1)[1]	1.10	2.64	3.638(7)	151

Symmetry codes: [1] 3/2-*x*, 1/2+*y*, 1/2+*z*.

Table S7. Hydrogen bond lengths [Å] and bond angles [°] of 5 at LTP.

D-H···A	D-H [Å]	H···A[Å]	D···A[Å]	D-H···A[°]
C(1)-H(1)···Cl(1)[2]	1.10	2.49	3.515(4)	154

Symmetry codes: [1] 1/2-*x*, 1/2+*y*, 1/2+*z*.

Table S8. The list of some typical molecular ferroelectrics with high phase transition temperatures.

Compound	**T_c (K)**	**Year**	**Reference**
(R)-3-quinuclidinol (S)-3-quinuclidinol	400/398	2018	[1]
2-(hydroxymethyl)-2-nitro-1,3-propanediol	362	2020	[2]
1,2,3,4,5-pentamethyl-6-nitrobenzene	403	2021	[3]
tris(4-acetylphenyl)amine	408	2021	[3]
D-*chiro*-inositol-$SiMe_3$	342	2022	[4]
(R)-BINOL-DIPASi/ (S)-BINOL-DIPASi	362/363	2022	[5]
R-CSAI and S-CSAI	429	2022	[6]
2-amino-2',4,4',6,6'-penta-fluoroazobenzene	443	2022	[7]
(−)-camphanic acid	414	2022	[8]
5-iodo-2-adamantanone	361	2022	[9]
tetrakis(4-fluorophenylethynyl)silane	475	2023	[10]
R_s-tBuSA/ S_s-tBuSA	348	2023	[11]
2,2,3,3,4,4-hexafluoropentane-1,5-diol	282	2024	[12]
B(9)-Br-$C_2B_{10}H_{11}$	353	2024	Our paper
B(9,12)-Br_2-$C_2B_{10}H_{10}$	437	2024	Our paper

Reference

1. P.-F. Li, W.-Q. Liao, Y.-Y. Tang, W. Qiao, D. Zhao, Y. Ai, Y.-F. Yao and R.-G. Xiong, Organic enantiomeric high-Tc ferroelectrics, *Proc. Natl. Acad. Sci.*, 2019, **116**, 5878-5885.
2. Y. Ai, Y.-L. Zeng, W.-H. He, X.-Q. Huang and Y.-Y. Tang, Six-Fold Vertices in a Single-Component Organic Ferroelectric with Most Equivalent Polarization Directions, *J. Am. Chem. Soc.*, 2020, **142**, 13989-13995.
3. S. Horiuchi, R. Kumai and S. Ishibashi, Single-component organic molecular ferroelectrics based on disk- or wheel-like rotation, *J Mater Chem C.*, 2021, **9**, 13739-13747.
4. Z. X. Zhang, X. J. Song, Y. R. Li, X. G. Chen, Y. Zhang, H. P. Lv, Y. Y. Tang, R. G. Xiong and H. Y. Zhang, The First Chiro-Inositol Organosilicon Ferroelectric Crystal, *Angew. Chem. Int. Ed. Engl.*, 2022, **61**, e202210809.
5. Y.-L. Zeng, Y. Ai, S.-Y. Tang, X.-J. Song, X.-G. Chen, Y.-Y. Tang, Z.-X. Zhang, Y.-M. You, R.-G. Xiong and H.-Y. Zhang, Axial-Chiral BINOL Multiferroic Crystals with Coexistence of Ferroelectricity and Ferroelasticity, *J. Am. Chem. Soc.*, 2022, **144**, 19559-19566.
6. P. F. Li, Y. Ai, Y. L. Zeng, J. C. Liu, Z. K. Xu and Z. X. Wang, Highest-T (c) single-component homochiral organic ferroelectrics, *Chem Sci*, 2022, **13**, 657-664.
7. H. Peng, J.-C. Qi, X.-J. Song, R.-G. Xiong and W.-Q. Liao, An unprecedented azobenzene-based organic single-component ferroelectric, *Chem. Sci.*, 2022, **13**, 4936-4943.
8. Y. Ai, P.-F. Li, M.-J. Yang, Y.-Q. Xu, M.-Z. Li and R.-G. Xiong, An organic plastic ferroelectric with high Curie point, *Chem. Sci.*, 2022, **13**, 748-753.
9. L. Xu, Y. Zhang, H. H. Jiang, N. Zhang, R. G. Xiong and H. Y. Zhang, Solvent Selective Effect Occurs in Iodinated Adamantanone Ferroelectrics, *Adv Sci (Weinh)*, 2022, **9**, e2201702.
10. H. Peng, H. Yu, S.-Y. Tang, Y.-L. Zeng, P.-F. Li, Y.-Y. Tang, Z.-X. Zhang, R.-G. Xiong and H.-Y. Zhang, High-Tc Single-Component Organosilicon Ferroelectric Crystal Obtained by H/F Substitution, *JACS Au*, 2023, **3**, 603-609.
11. H. Peng, Z. K. Xu, Y. Du, P. F. Li, Z. X. Wang, R. G. Xiong and W. Q. Liao, The First Enantiomeric Stereogenic Sulfur-Chiral Organic Ferroelectric Crystals, *Angew. Chem. Int. Ed. Engl.*, 2023, **62**, e202306732.
12. H. Y. Zhang, Y. Y. Tang, Z. X. Gu, P. Wang, X. G. Chen, H. P. Lv, P. F. Li, Q. Jiang, N. Gu, S. Ren and R. G. Xiong, Biodegradable ferroelectric molecular crystal with large piezoelectric response, *Science*, 2024, **383**, 1492-1498.

NMR

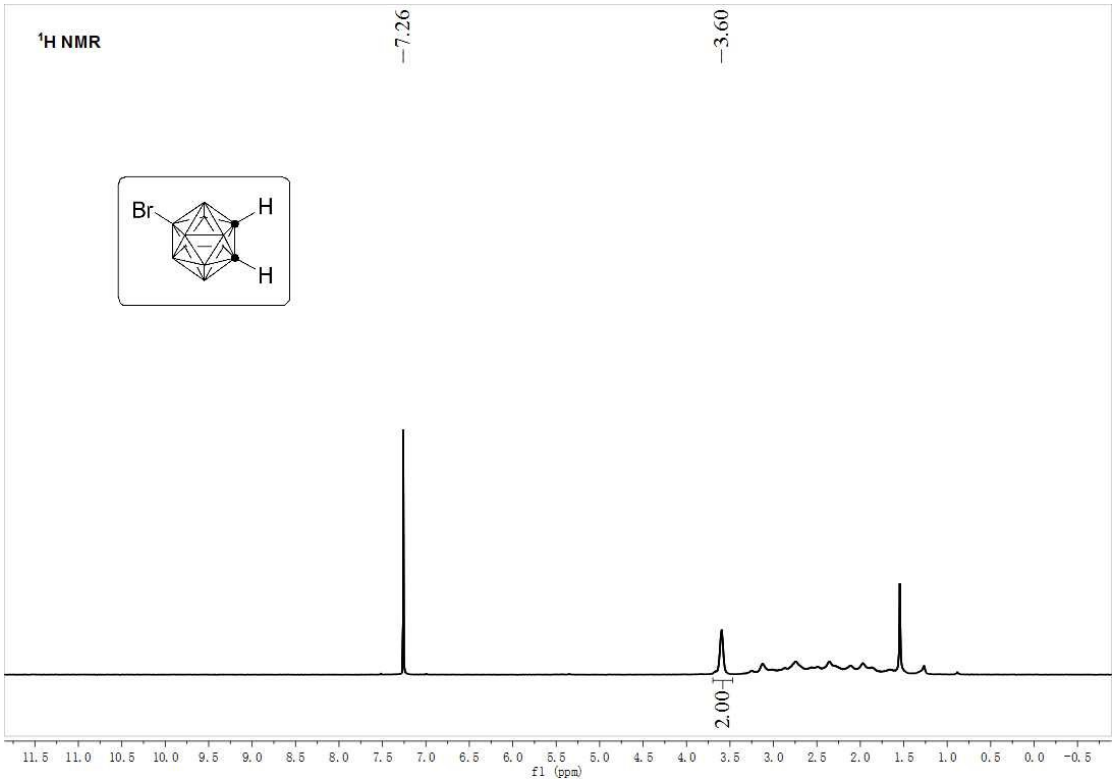
^{1}H NMR
7.26
3.60
Br
H
H
2.00
11.5 11.0 10.5 10.0 9.5 9.0 8.5 8.0 7.5 7.0 6.5 6.0 5.5 5.0 4.5 4.0 3.5 3.0 2.5 2.0 1.5 1.0 0.5 0.0 -0.5
f1 (ppm)

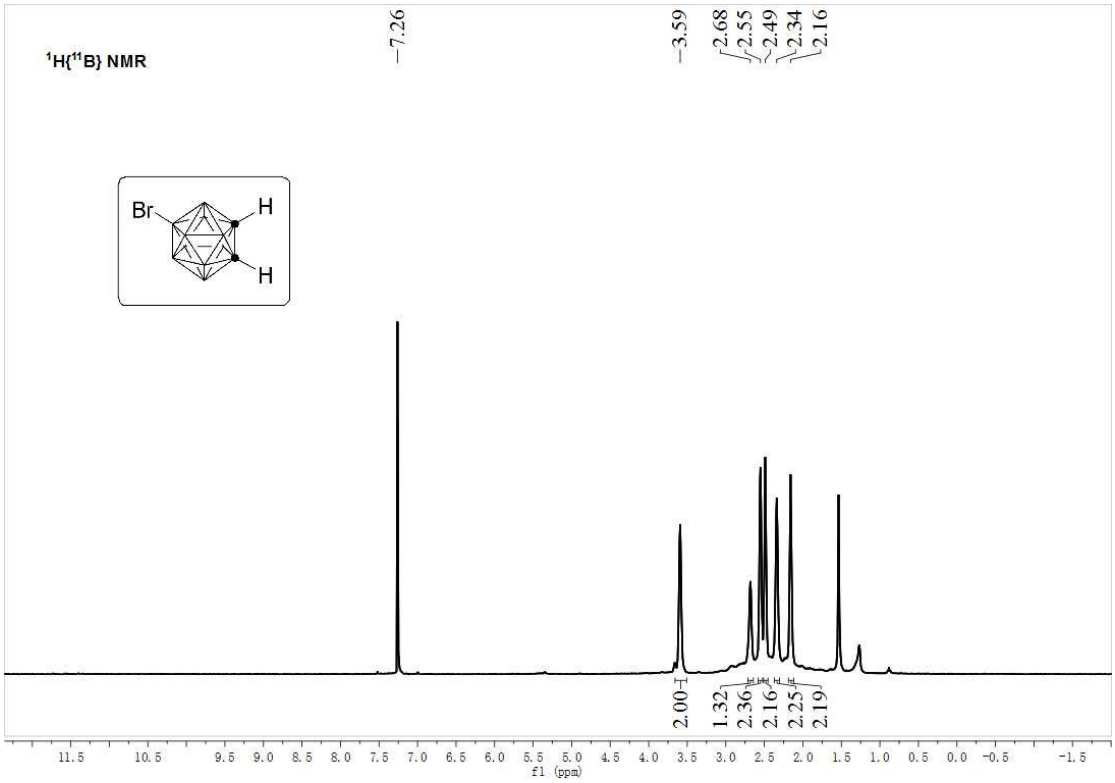
^{1}H{^{11}B} NMR
7.26
3.59
2.68
2.55
2.49
2.34
2.16
Br
H
H
2.00
1.32
2.36
2.16
2.25
2.19
11.5 10.5 9.5 9.0 8.5 8.0 7.5 7.0 6.5 6.0 5.5 5.0 4.5 4.0 3.5 3.0 2.5 2.0 1.5 1.0 0.5 0.0 -0.5 -1.5
f1 (ppm)

^{11}B NMR

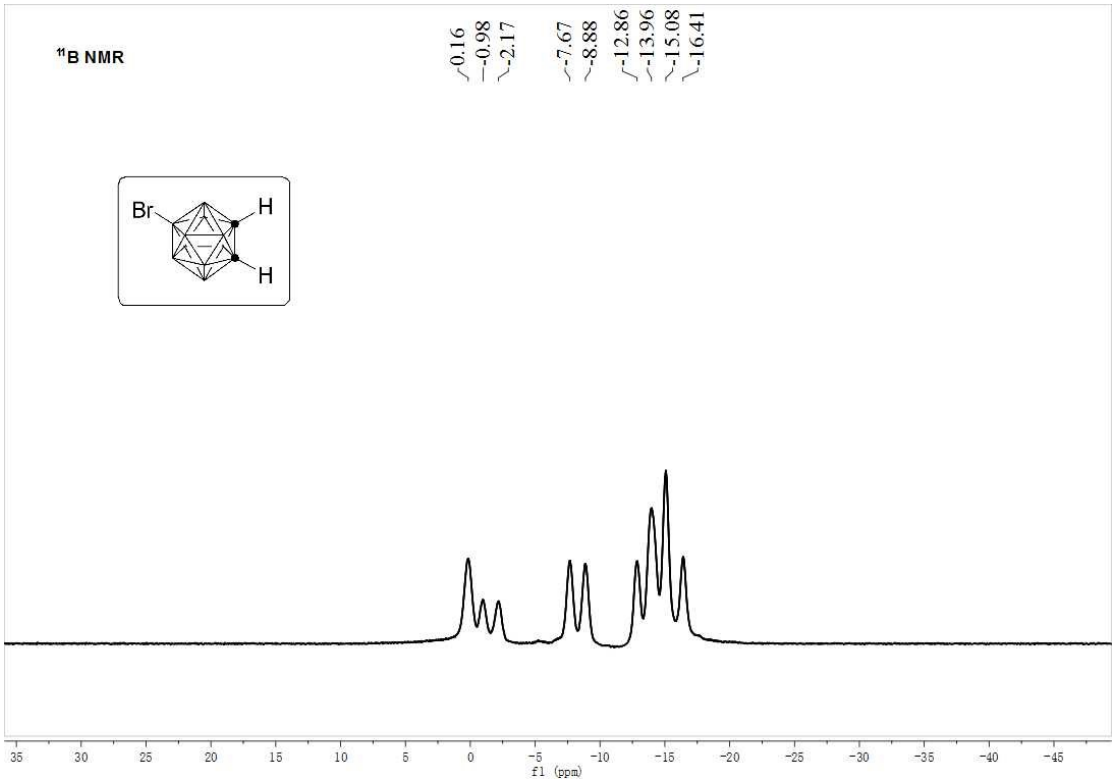

^{11}B{^{1}H} NMR

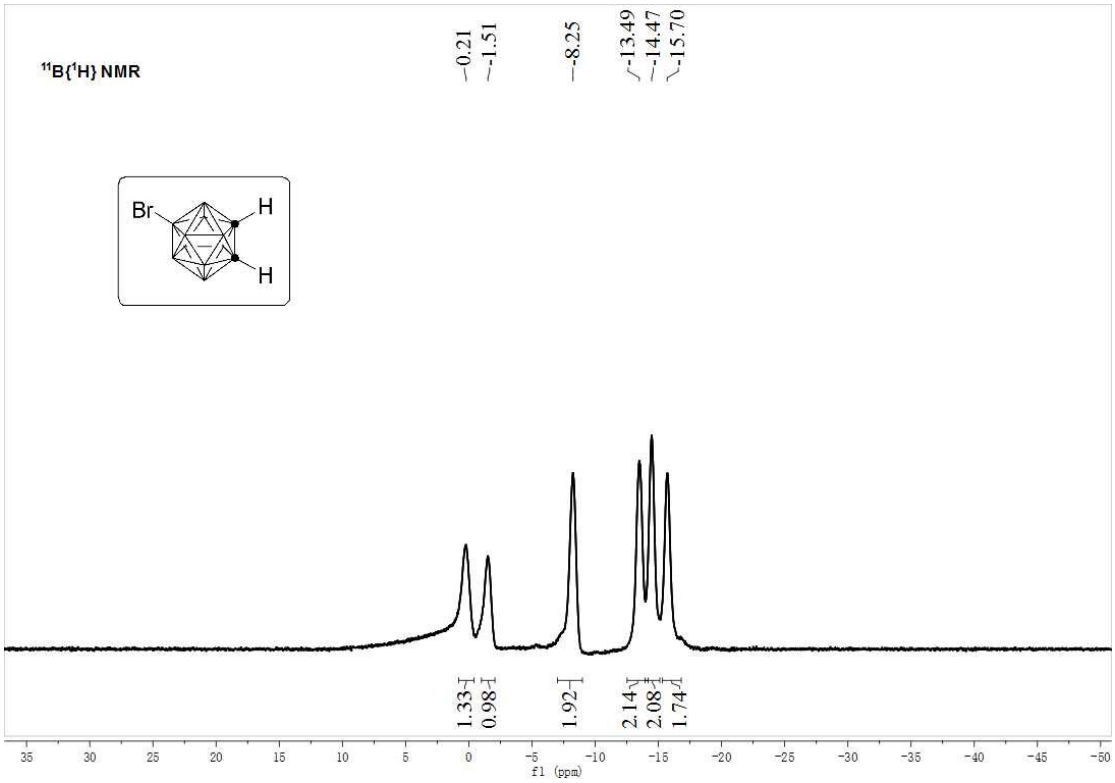

^{13}C NMR

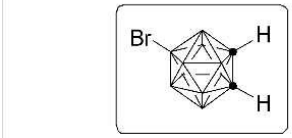

^{1}H NMR

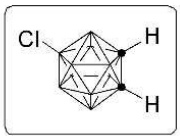

$^{1}H\{^{11}B\}$ NMR

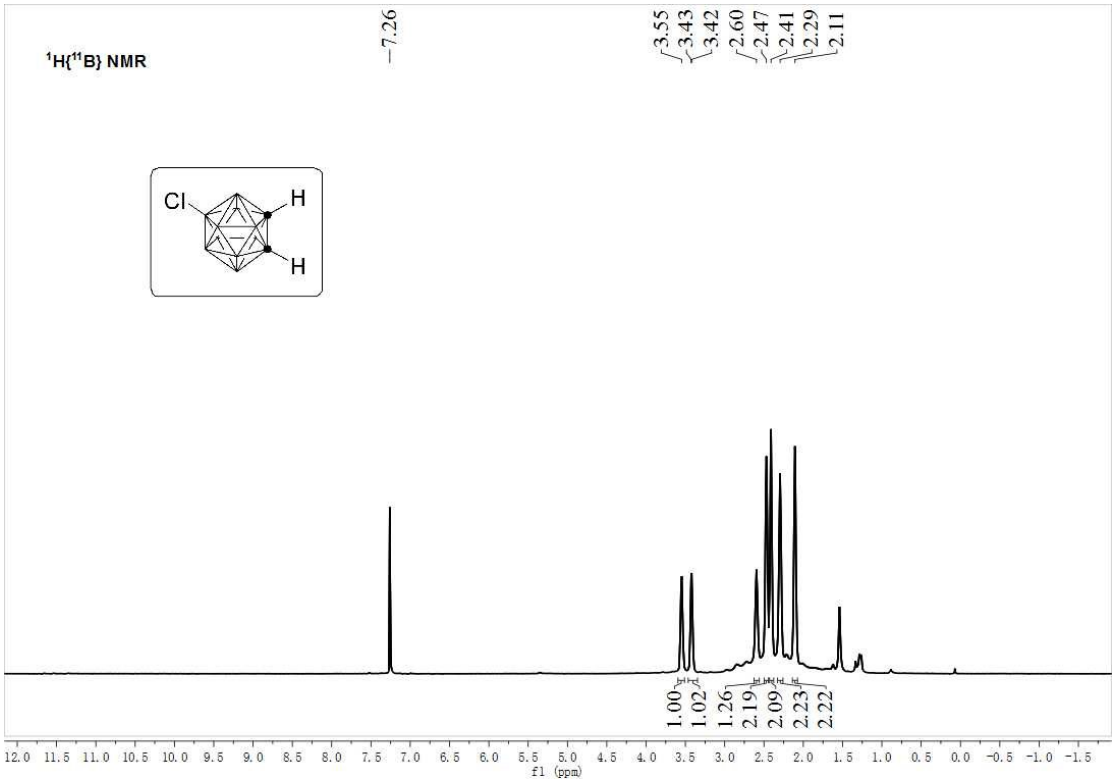

^{11}B NMR

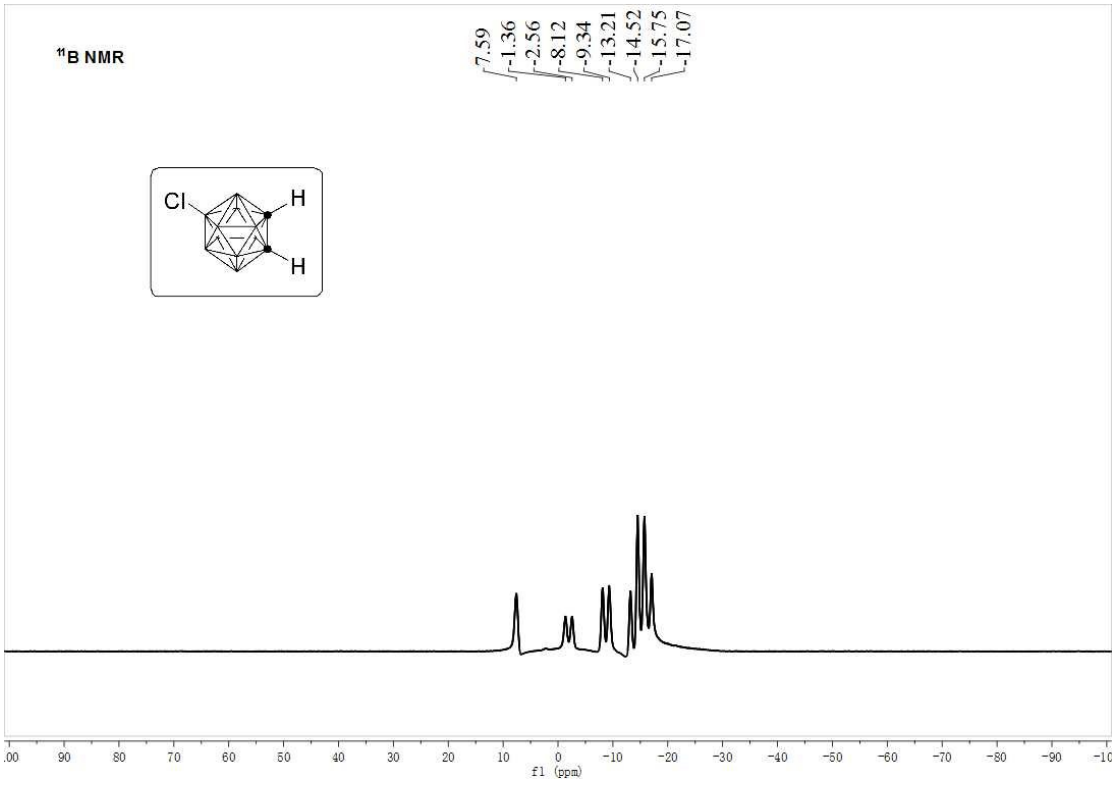

$^{11}B\{^{1}H\}$ NMR

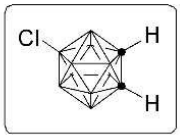

^{13}C NMR

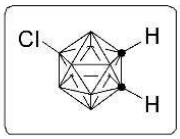

^{1}H NMR

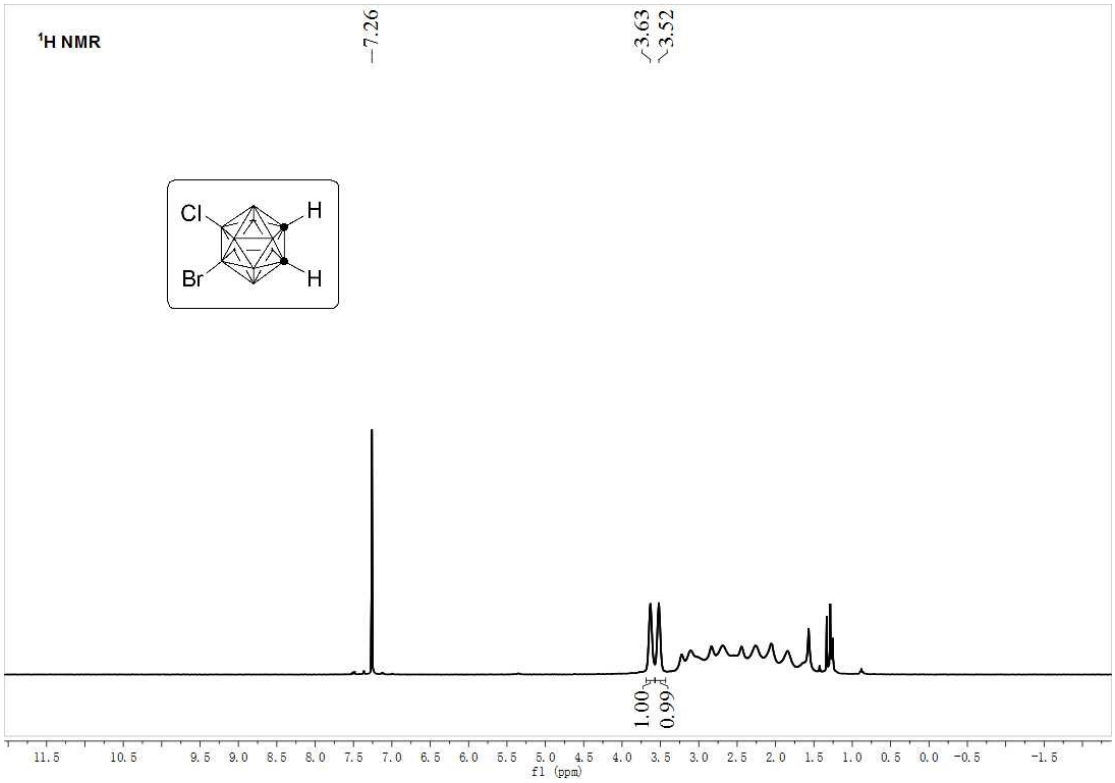

^{1}H{^{11}B} NMR

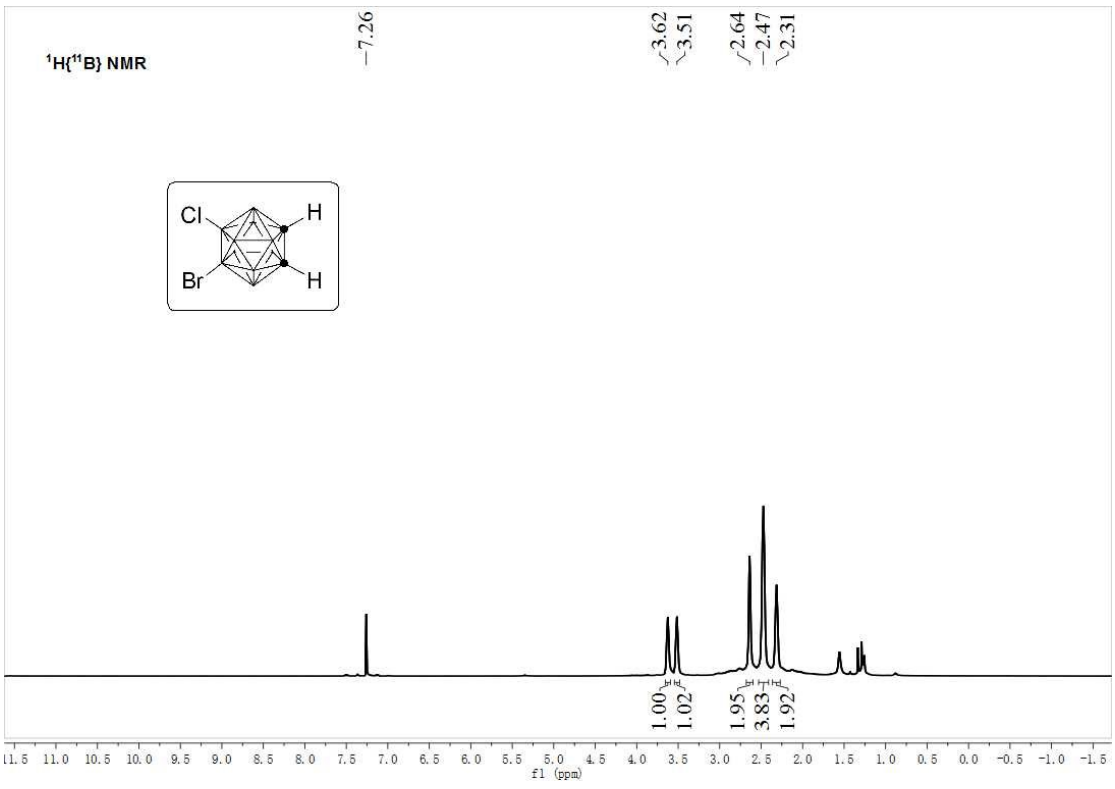

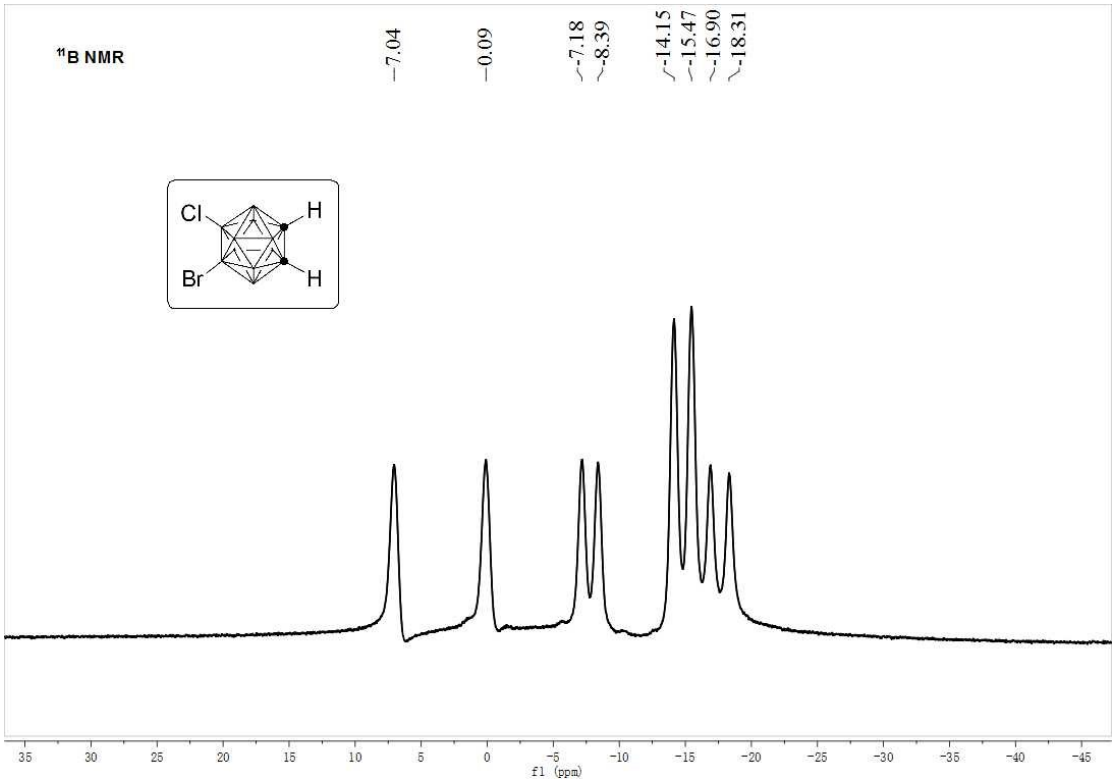
^{11}B NMR
-7.04
-0.09
-7.18
-8.39
-14.15
-15.47
-16.90
-18.31
Cl
H
Br
H
f1 (ppm)

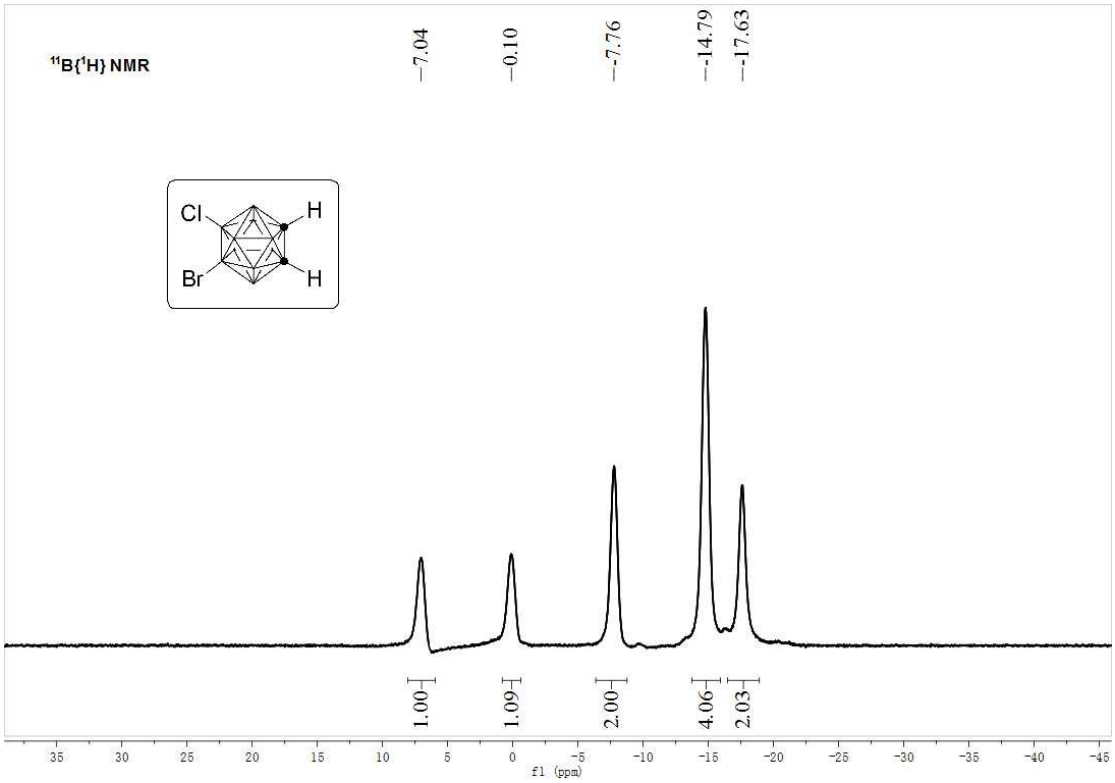
^{11}B{^{1}H} NMR
-7.04
-0.10
-7.76
-14.79
-17.63
Cl
H
Br
H
1.00
1.09
2.00
4.06
2.03
f1 (ppm)

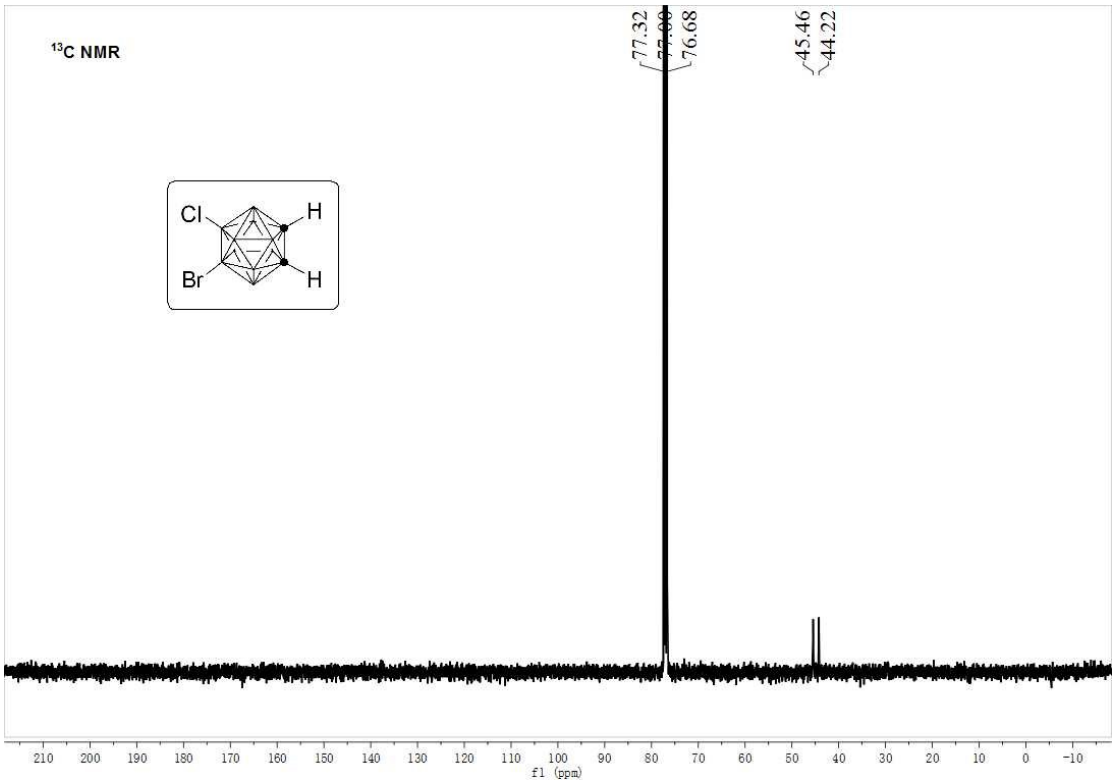
^{13}C NMR
77.32
76.68
45.46
44.22
Cl
H
Br
H
f1 (ppm)

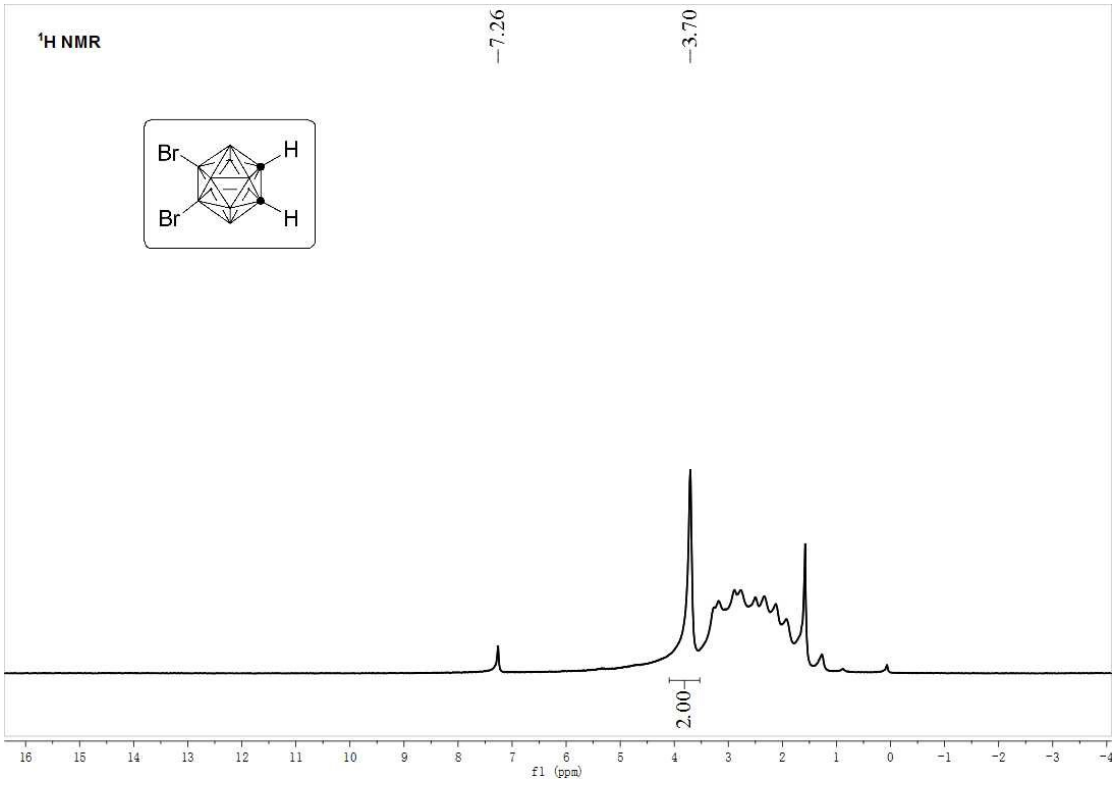
^{1}H NMR
7.26
3.70
Br
H
Br
H
2.00
f1 (ppm)

$^{1}H\{^{11}B\}$ NMR

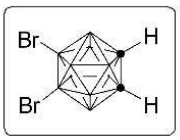

^{11}B NMR

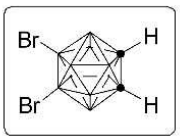

$^{11}B\{^{1}H\}$ NMR

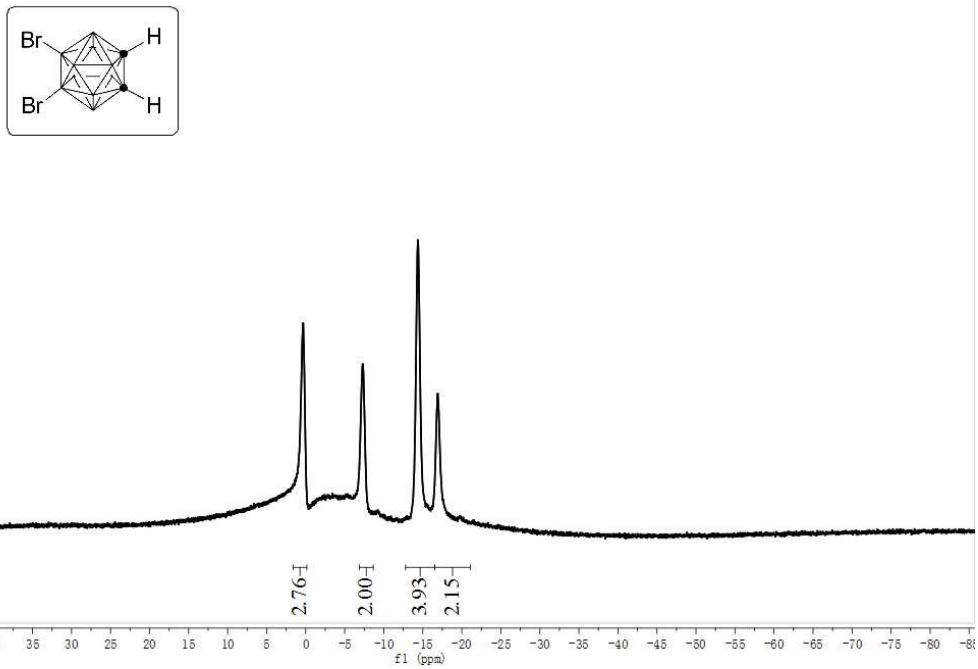

^{13}C NMR

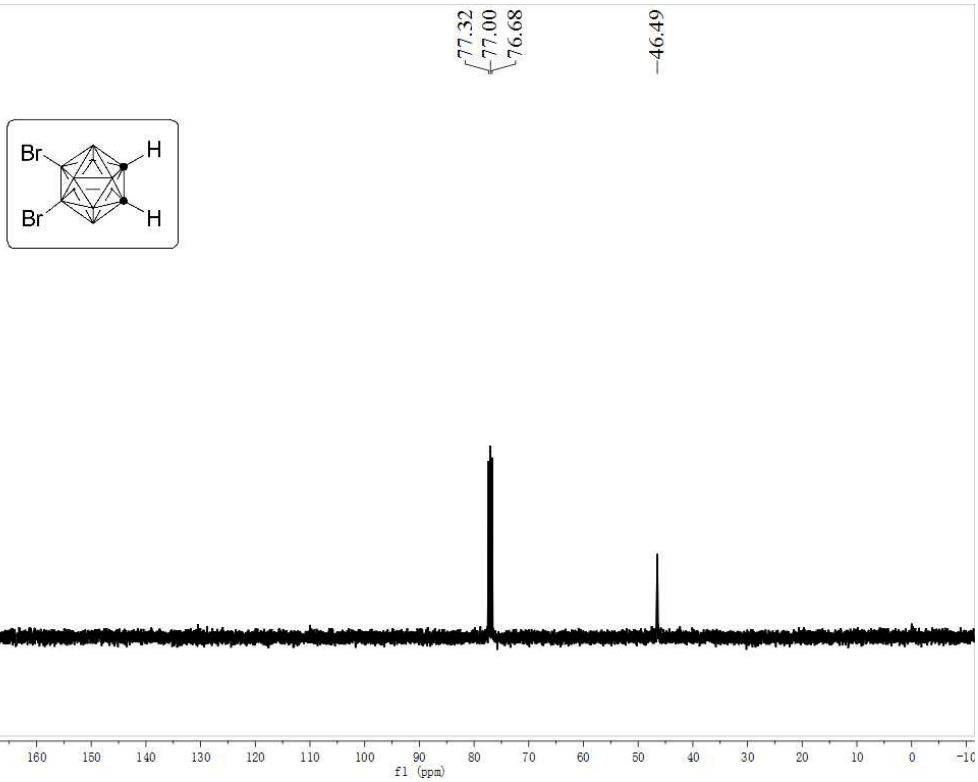

^{1}H NMR

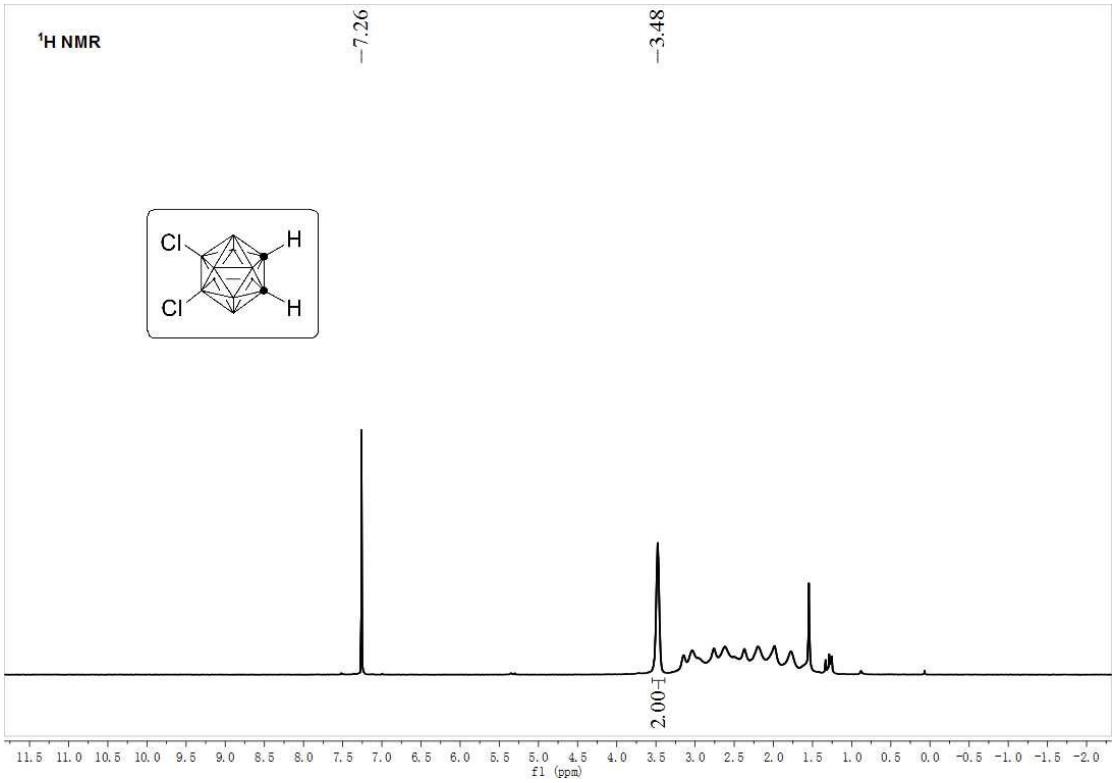

^{1}H{^{11}B} NMR

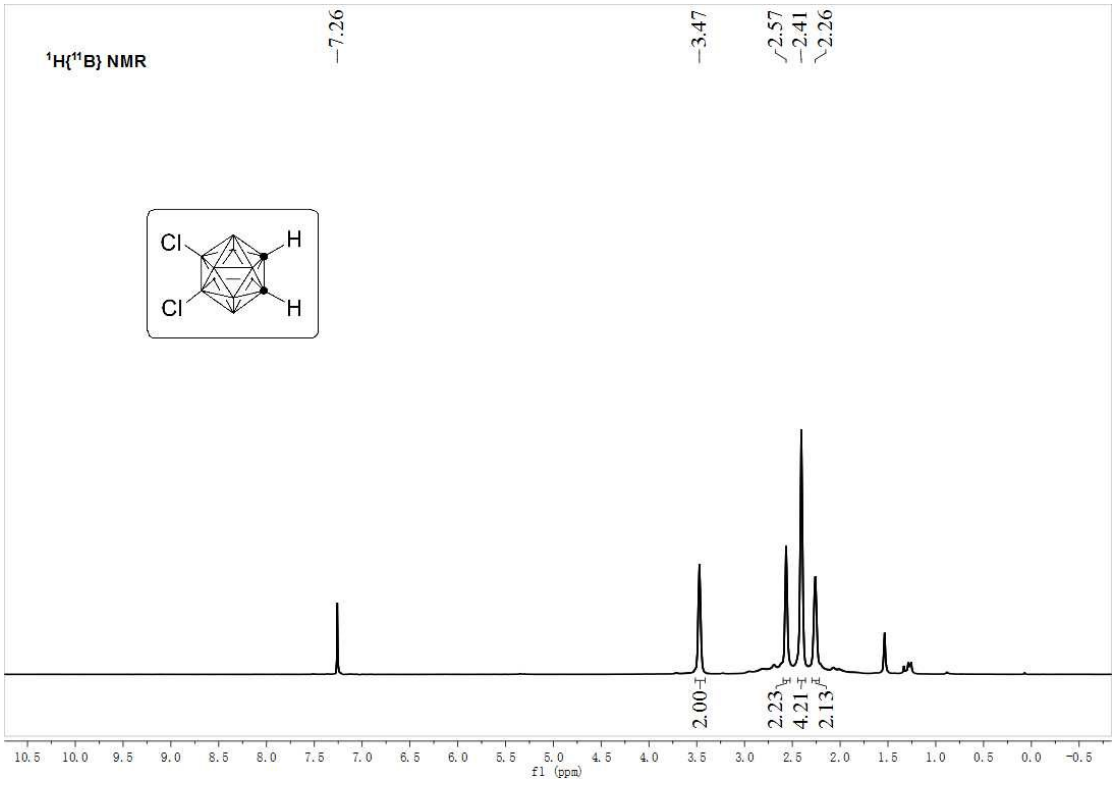

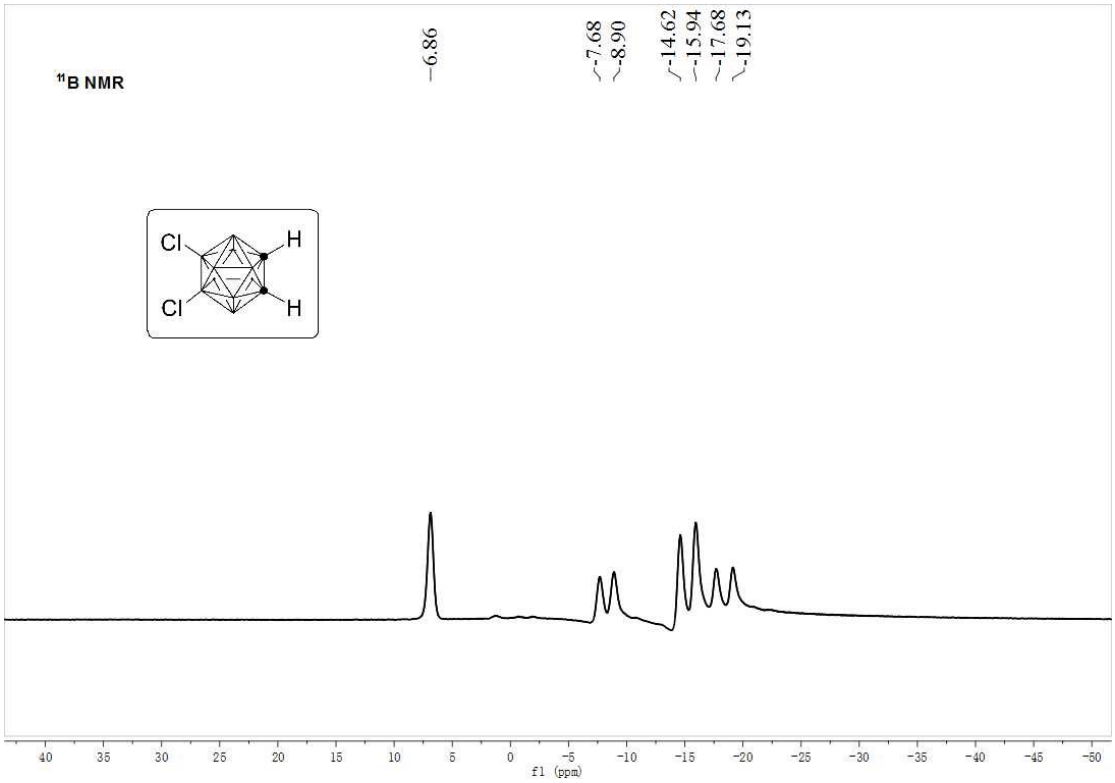
^{11}B NMR
-6.86
-7.68
-8.90
-14.62
-15.94
-17.68
-19.13
Cl
H
Cl
H
40 35 30 25 20 15 10 5 0 -5 -10 -15 -20 -25 -30 -35 -40 -45 -50
f1 (ppm)

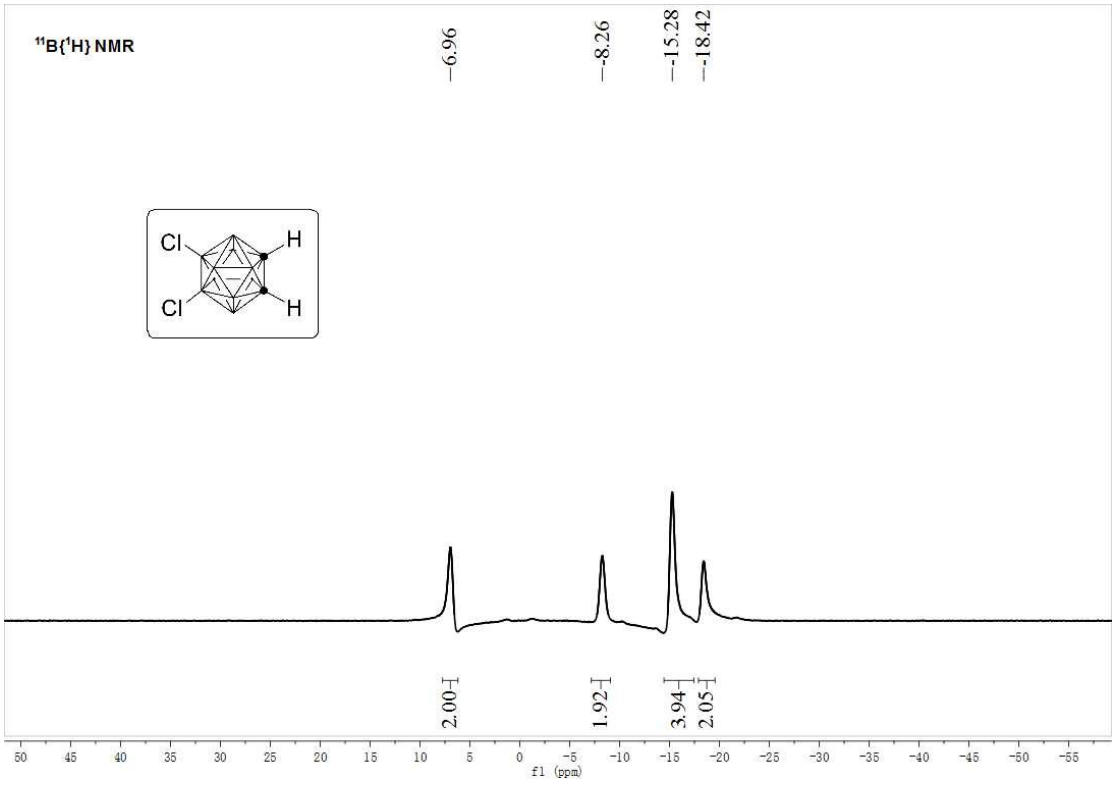
^{11}B{^{1}H} NMR
-6.96
-8.26
-15.28
-18.42
Cl
H
Cl
H
2.00
1.92
3.94
2.05
50 45 40 35 30 25 20 15 10 5 0 -5 -10 -15 -20 -25 -30 -35 -40 -45 -50 -55
f1 (ppm)

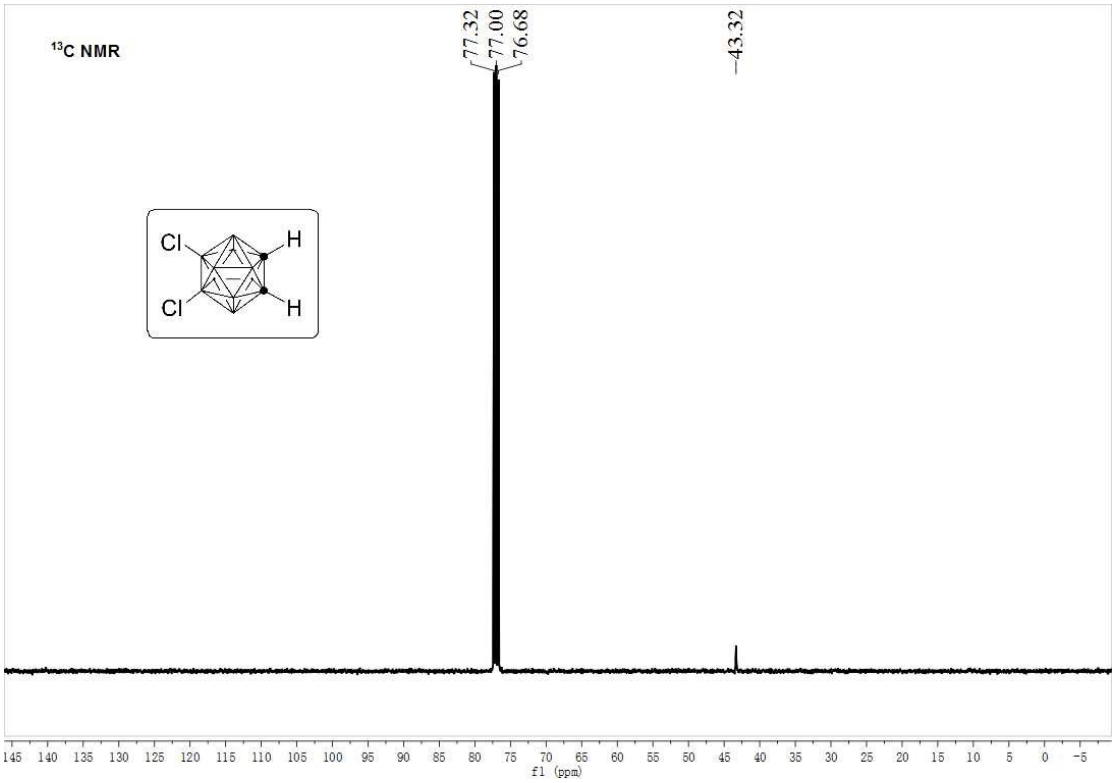
^{13}C NMR
77.32
77.00
76.68
43.32
Cl
H
Cl
H
145 140 135 130 125 120 115 110 105 100 95 90 85 80 75 70 65 60 55 50 45 40 35 30 25 20 15 10 5 0 -5
f1 (ppm)